MICROSTRUCTURAL AND MECHANICAL CHARACTERIZATION OF AS-CAST NICKEL-BASED SUPERALLOY (IN-713C)

M. F. Moreira and **L. B. Fantin**

Center for Metallurgical and Materials Technologies, Institute for the Technological Research of the State of São Paulo (IPT), São Paulo, SP, Brazil

M. F. Moreira, L. B. Fantin, F. Beneduce Neto and C. R. F. Azevedo

Department of Metallurgical and Materials Engineering, Polytechnic School of the University of São Paulo, São Paulo, SP, Brazil

Abstract

Inconel 713C as-cast test pieces were produced by investment casting. The tensile properties at 25 and 650 °C were obtained along with microstructural and microfractographic characterization. The tensile testing results followed the requirements of the AMS 5391D standard. Additionally, stress-rupture testing at 982 °C and 152 MPa, and 815 °C and 305 MPa was carried. The aged $\gamma - \gamma'$ microstructures were compared and discussed in terms of rafting kinetics. The stress-rupture results followed the AMS 5391D requirements. The relationship between the as-cast and aged microstructures and the mechanical properties was discussed.

Keywords: *IN-713C Ni superalloy, Mechanical testing, Microstructure, Thermal exposure, Rafting*

Introduction

Nickel-based superalloys are used at elevated temperatures due to their excellent mechanical properties and oxidation resistance.[1–3] Wrought nickel-based superalloys feature superior tensile strength (up to 1600 MPa for Rene 95) and ductility (up to 55%, IN 617) when compared to cast nickel-based superalloys (tensile strength up to 1200 MPa for MAR M432, and ductility up to 14%, for IN-713LC). The microstructure of cast Ni-based superalloys combines the γ matrix with a proportion of coherent γ' (Ni$_3$Al) submicron precipitates along with primary carbides and borides.[1–3] Inconel 713C (IN-713C) was the first of several cast nickel–chromium-based superalloys developed by the International Nickel Company during the 1940s.[4,5] In this sense, some parts of the aircraft turbine present a complex geometry, which does not allow the intensive use of machining processes, favoring the investment casting process. This process's low cooling rate is suitable for the production of parts with large grain sizes, excellent surface quality and dimensional precision.[1–3,6,7] IN-713C cast alloy is popular due to its appropriate castability, good tensile properties and maximum service temperature around 980 °C, allied to suitable oxidation and thermal fatigue resistance.[4–19] The mechanical properties are mainly controlled by the $\gamma - \gamma'$ duplex microstructure, and improved stress-rupture life can be obtained by solution heat treatment.[4,20–27]

Thermodynamic equilibrium calculation (see Figure 1a) shows a solidification sequence of IN-713C alloy taking place in a 75 °C interval: $L \rightarrow L + \gamma \rightarrow L + \gamma + MC \rightarrow L + \gamma + MC + M_3B_2$. Few studies using thermal analysis reported the formation of the MC carbide (M = Nb, Mo, Zr and Ti, FCC structure) before the γ dendrites.[13] The thermodynamic modeling of IN-713LC using a Scheil–Gulliver solidification simulation is shown in Figure 1b. This simulation indicated a different solidification sequence taking place in a broader interval ($\sim$ 200 °C): $L \rightarrow L + \gamma \rightarrow L + \gamma + MC \rightarrow L + \gamma + MC + M_3B_2 \rightarrow L + MC + M_3B_2 + \gamma + \gamma'$. In these conditions, the segregation of C, Mo, Zr, Cr, Nb, B, Al and Ti to the interdendritic liquid forms "non-equilibrium
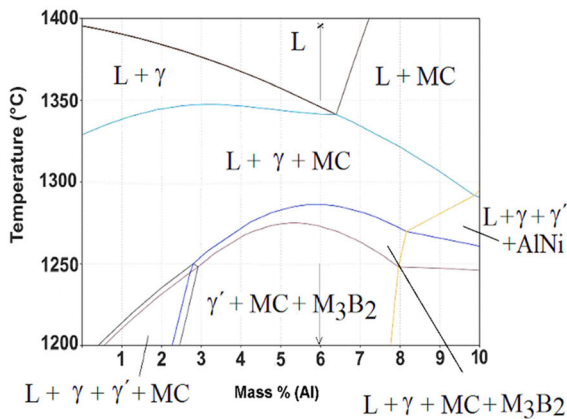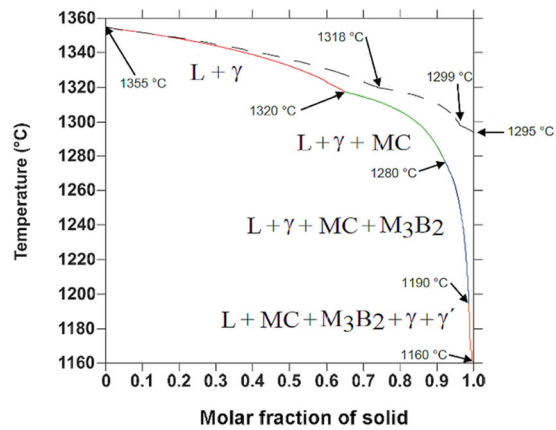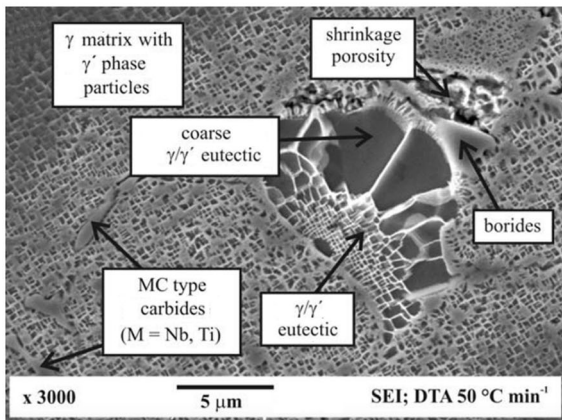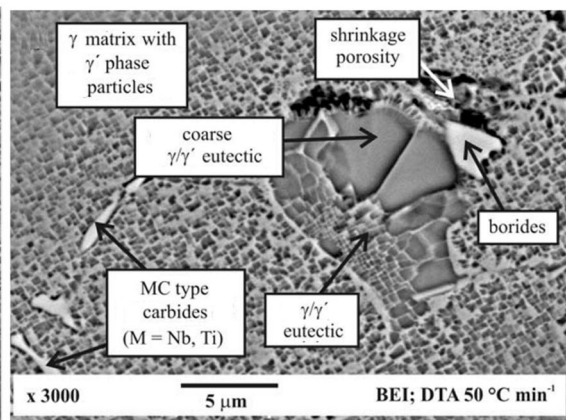
Figure 1. *(a) Quasibinary Ni–Al phase diagram for IN-713C base composition, using Thermo-Calc software; (b) phase equilibria and Scheil–Gulliver solidification of IN-713LC alloy, using Thermo-Calc software;[10] (c) and (d) as-cast microstructure of the IN-713LC alloy characterized by γ dendrites with γ′ precipitation, interdendritic γ − γ′ eutectic, MC carbides and borides, SEM, SEI and BEI.[9] (c) and (d) were used with permission of Springer Nature Customer Service Centre GmbH: Springer Nature; Journal of Thermal Analysis and Calorimetry, S. Zlá et al., Determination of thermophysical properties of high-temperature alloy IN713LC by thermal analysis, © 2012.*

eutectics" during the solidification. The as-cast microstructure of IN-713C alloy (see Figure 1c and d) presents, therefore, primary γ dendrites with coherent cubic γ′ precipitates, and interdendritic MC carbide, γ − γ′ eutectic and boride particles.[7–18]

Thermal exposure during service conditions causes the partial decomposition of the MC carbide, followed by the precipitation of $M_{23}C_6$-type carbides (M = Cr, Mo and Ti, FCC), see Figure 2a and b.[7–18,20,21,26,27] The decomposition of Nb-rich MC carbide causes the diffusion of Nb into the adjacent matrix, promoting the Nb-stabilization of the γ′ phase, leading to the formation of γ′ pools around the $M_{23}C_6$ carbides: MC + γ → ($M_{23}C_6$ + γ′). The precipitation of M_6C and two types of MC carbides (see Figure 2b) during the thermal exposure[14,24,26] has not

been confirmed by thermodynamic equilibrium calculation (see Figure 2c). Prolonged thermal exposure at temperatures below 900 °C causes the precipitation of needle-like σ phase (tetragonal, usually rich in Ni, Cr and Mo) after 400 h at 815 °C (see Figure 2a and b).[18,24,26] The coherent γ′ precipitates show a cube–cube orientation relationship with the γ matrix, and the proportion of γ and γ′ phases in the microstructure varies significantly with the temperature (see Figure 2c). In the absence of applied stress, the coarsening of the cuboid γ′ precipitates during the thermal exposure occurs without much change in the cuboid morphology.
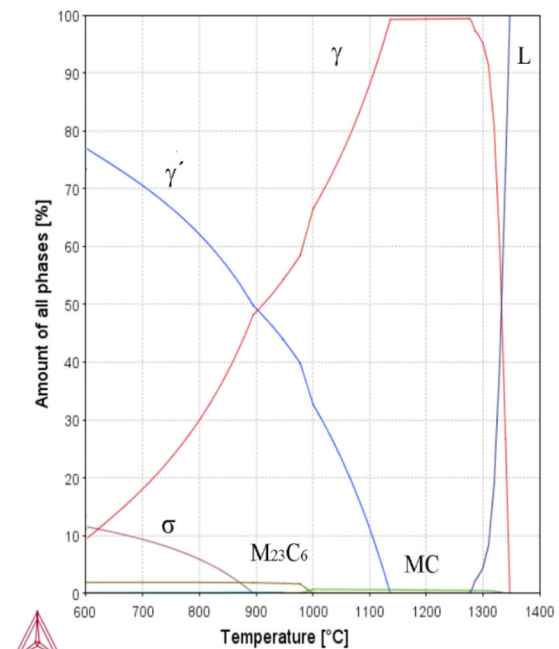
In the presence of applied stress, directional coarsening of the cuboid γ′ precipitates takes place, and the coherent γ′ precipitates grow into a plate morphology, known as rafts.
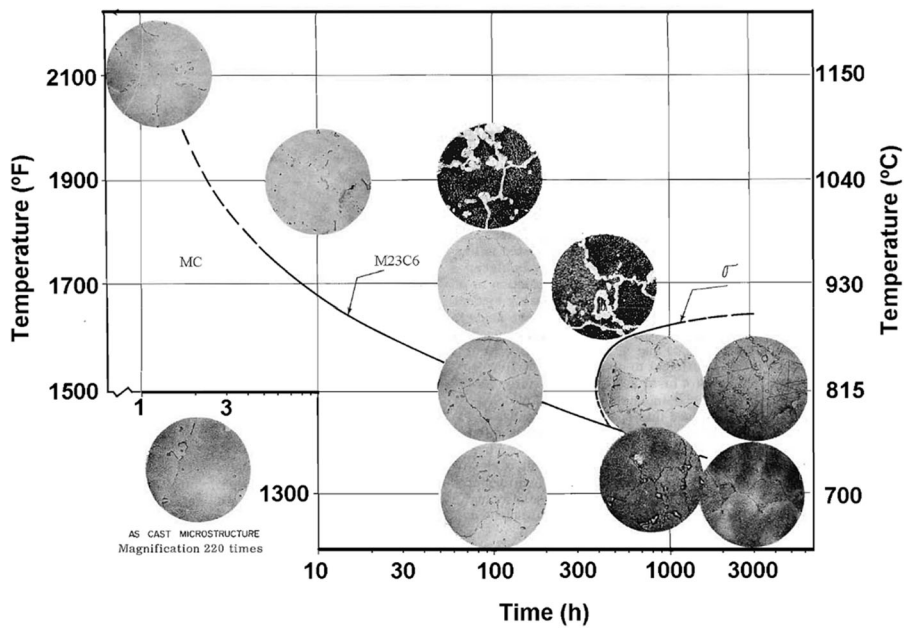
(a)
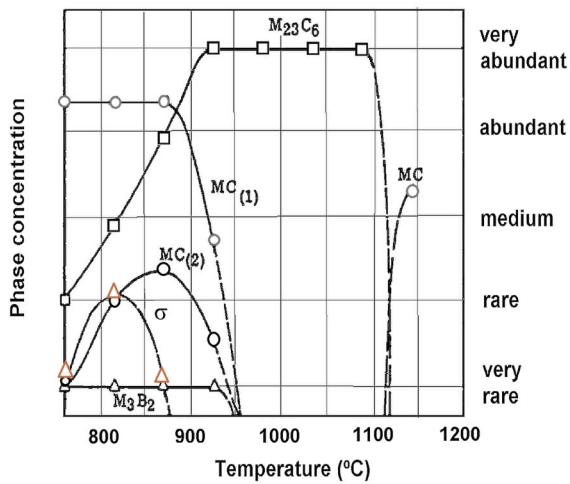
(b)

(c)

Figure 2. (a) Thermal exposure, TTT curve for an as-cast IN-713C alloy (electron vacancy number, Nv, equals to 2.10), showing the start of the M$_{23}$C$_6$ and σ phase precipitation;[18,24] (b) minor phase concentration in IN-713C as a function of temperature for long exposure times (2000–5000 h)[24,26]; (c) phase concentration in equilibria in IN-713C alloy as a function of temperature, Thermo-Calc software. (a) Used with permission of The Minerals, Metals & Materials Society; Transactions of the Metallurgical Society of AIME, Mihalisin et al., Sigma—its occurrence, effect, and control in nickel-based superalloys, © 1968. (b) Was used with the permission of The Minerals, Metals and Materials Society; Proceedings of the International Symposium on the Structural Stability in Superalloys, H. E. Collins, Relative long-time stability of carbide and intermetallic phases in nickel-based superalloys, © 1968.

The rafting orientation depends on the type and direction of the applied load, the $\gamma - \gamma'$ elastic modulus mismatch and the lattice parameter $\gamma - \gamma'$ misfit, δ, where $\delta = (a_{\gamma'} - a_{\gamma})/a_{\gamma}$.[1–3,28–35] The elastic inhomogeneity implies that most of the elastic deformation caused by the $\gamma - \gamma'$ misfit is located in the γ phase near the $\gamma - \gamma'$ coherent interfaces, and the compressive coherency stress in the γ channels can reach values around 500 MPa (see Figure 3a). Most commercial Ni-based superalloys present a negative $\gamma - \gamma'$ misfit (around 0.03%) at high temperatures, indicating that these γ channels will be under compressive coherency stress. The presence of external tensile stress (350 MPa at 950 °C) reduces the compressive stress in the vertical γ channels, but it increases the compressive stress up to 800 MPa in the horizontal γ channels, see Figure 3b. This rise in the compressive stress promotes the creep and plastic deformation of the horizontal γ channels, generating $\gamma - \gamma'$ interfacial dislocations, which relax the interfacial misfit and locally minimize the compressive stress. The driving force for the atomic diffusion and the rafting is, therefore, the elastic strain energy gradient between the vertical and horizontal γ channels, see Figure 3c.[28] The rafting kinetics is influenced by the slow diffusion elements, the temperature, the volumetric fraction of γ' phase, the magnitude of the applied external stress or the prior plastic deformation, the $\gamma - \gamma'$ lattice misfit, the $\gamma - \gamma'$ elastic inhomogeneity and the elastic strain energy gradient between the horizontal and vertical γ channels.[1–3,28–35]

The present paper will assess the macro- and microstructures, the tensile properties at 25 and 650 °C, the stress-rupture properties (152 MPa and 982 °C, and 305 MPa and 815 °C) of IN-713C as-cast test pieces produced by investment casting.

Methods

Figure 4a shows the wax pattern assembly design, and the model consists of a pouring cup, a central sprue, and nine stress-rupture test pieces per mold. Figure 4b indicates the dimensions of the test piece. Zircon sand (primary and back-up slurries), 70# and 140# zircon grains (primary *stucco*), 20# and 50# aluminum–silicate grains (back-up *stucco*), and sodium-stabilized colloidal silica (binder for the primary and back-up slurries) were used for the production of the ceramic molds. The molding procedure consisted of the application of a first coat, followed by air-drying for 60 min (temperature: 22 °C; relative humidity: 60%) and the use of four secondary coatings, each one, except for the last, followed by air-drying during 60 min (temperature: 22 °C; relative humidity: 45%). Final air-drying took 32 h (temperature: 22 °C; relative humidity: 45%), followed by dewaxing in the steam autoclave at 120 °C and firing at 1050 °C for 1.5 h. The samples were conventionally cast in a vacuum induction furnace (Daido Steel vacuum induction furnace with 5 kg capacity, 20 kW

power and 9 kHz frequency) using pre-formed alumina crucible and Cannon Muskegon IN-713C stock bars. The pressure in the furnace during the melting process was kept between 0.04 and 0.09 Pa. The experimental assembly allowed the measurement of the molten metal and the ceramic mold temperatures. Ceramic molds were heated in a second induction furnace with a graphite susceptor, and two thermocouples in a loop-circuit controlled the mold temperature. The pouring temperature was initially set up at 1500 °C (about 110 °C of superheating) and ceramic mold temperature at 1100 °C (temperature, which produced complete filling of test pieces). The alloying and residual elements were chemically analyzed by wavelength-dispersive X-ray fluorescence spectrometry (Shimadzu Lab Center XRF 1800), ICP (Inductively Coupled Plasma Shimadzu ICPQ(V)-1014) and atomic absorption spectrophotometry (PerkinElmer, AA 703).

Tensile tests were performed at room temperature and 650 °C (20 min soaking time) using an electro-mechanical MTS/Sintech 30D testing machine and following the requirements of ASTM E8[36] and ASTM E21[37] standards. Stress-rupture testing at 815 °C (load of 305 MPa) and 982 °C (load of 152 MPa) was carried out using constant-load creep machines. The results were compared against the requirements of AMS 5391D[38] standard. The metallographic samples were macroetched with a solution of 3 parts of HCl and 1 part of H_2O_2. Glyceregia etchant (30 ml glycerol, 20 ml HCl, 10 ml HNO_3) was employed for the microstructural examination. Microstructural characterization was performed by stereomicroscope (Carl Zeiss Jena Technival 2), optical microscope (Olympus BX51 optical microscope) and scanning electron microscopes (FEI Quanta 400, JEOL JSM 6300 and JEOL JSM 5200, all equipped with EDS microanalysis). EDS microanalyses were carried out using dual beam Quanta 3D FEG-SEM, EDAX APEX^{TM} software, standardless mode, point analysis, acquisition time of 200 s and 20 kV accelerating voltage. The volume fractions of interdendritic $\gamma - \gamma'$, primary carbides and γ' precipitates were measured by ImageJ software (National Institute of Health, 1.52 version). Finally, the equilibrium and Scheil–Gulliver simulations of the IN-713C alloy solidification sequence used the chemical composition results (see Table 1) and Thermo-Calc software (Ni data version 6).

Results and Discussion

Table 1 shows the chemical composition of DV 106 and DV 109 heats and the requirements of the AMS 5391D standard.[38] Most results follow the specification, except for the Cr content, which is slightly above the maximum limit. Figure 5a brings a general view of the as-cast creep test pieces (diameter of 6.0 mm) after macroetching to evaluate the grain size and grain size distribution. The grain size distribution is homogeneous. Figure 5b shows a
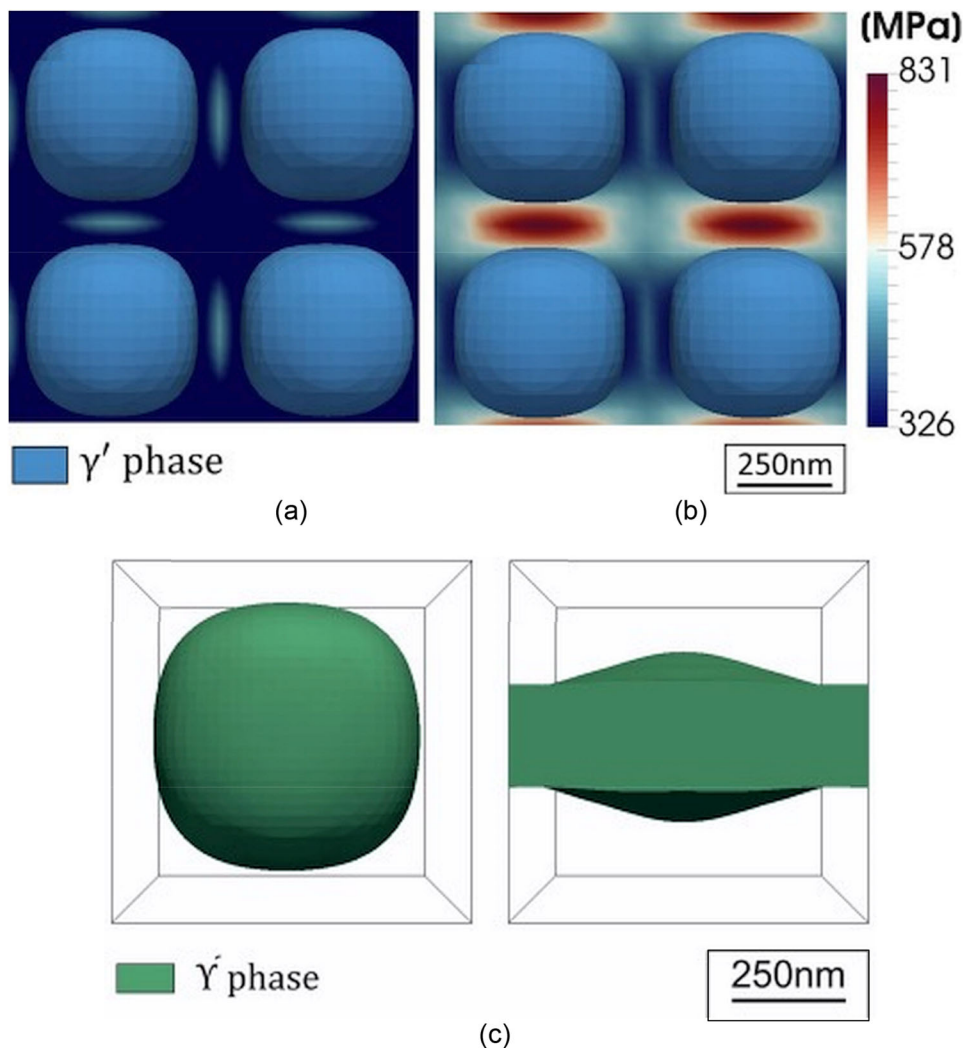
Figure 3. Simulated compressive stress distribution in the γ channels located between the four γ' cuboid precipitates for a negative $\gamma - \gamma'$ misfit. (a) Without the presence of external stress, the vertical and horizontal γ channels feature similar von Mises coherency stresses[28]; (b) stress distribution in the γ channels under an external tensile stress of 350 MPa at 950 °C. The compressive stresses are relieved in the vertical γ channels, while the compressive stresses in the horizontal γ channels are increased; (c) simulation results of a single γ' particle (green color). Initial cubic morphology (left)—subjected to a tensile stress of 350 MPa at 950 °C— presents γ' particle directional growth (rafting, see right) during the creep aging.[28] (a) to (c) were used with permission of Elsevier; Computational Materials Science, M. Ali et al., Role of coherency loss on rafting behavior of Ni-based superalloys, © 2020.

representative transversal macrography of an as-cast test piece, featuring equiaxial grains with an average size of approximately 1400 μm and volume fraction of pores equal to 0.2%.

Figure 6a and b shows that the as-cast microstructure presents fine and coarse interdendritic non-equilibrium $\gamma - \gamma'$ eutectic, see arrow 2, and interdendritic faceted MC carbides (around 1% in volume), see arrow 1. The EDS microanalysis of the MC carbide indicated the predominant presence of Nb, Ti and Mo, see Table 2. Figure 1b indicates that the formation of the interdendritic eutectic $\gamma - \gamma'$

structure is the last to occur during the IN-713LC alloy's solidification. According to the Warnken,[42] however, the distinction of whether this interdendritic $\gamma - \gamma'$ structure is formed by a peritectic or eutectic reaction is not straightforward. Therefore, the present work uses the term interdendritic $\gamma - \gamma'$ until this dispute is over, and the volumetric fraction of the interdendritic $\gamma - \gamma'$ structure is around 5%. Previous investigation[43–45] on Ni-superalloy single crystals' solidification path indicated that the fine interdendritic $\gamma - \gamma'$ structure was formed before the coarse structure. The coarse interdendritic $\gamma - \gamma'$ structure in Figure 6b (arrow 2) is likely formed by the continuous
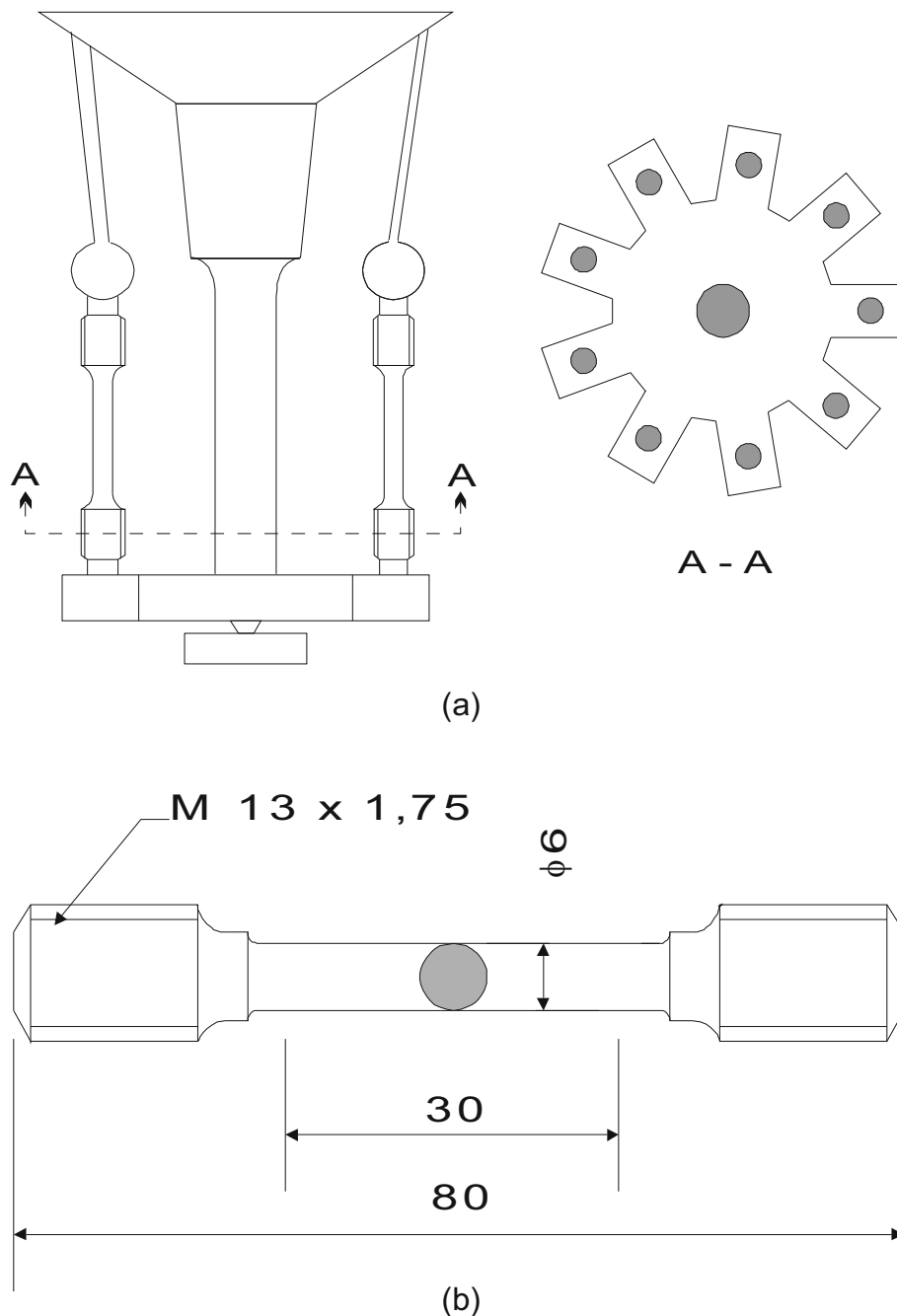
Figure 4. *(a) Design of the wax pattern assemble; (b) dimensions of as-cast test pieces (mm).*

growth of the fine interdendritic $\gamma - \gamma'$ structure, mainly by the preferential growth of the γ' phase. Wang et al.[44] proposed that the latent heat released during the formation of the fine $\gamma - \gamma'$ eutectic cells increased the liquid temperature and decreased the nucleation undercooling, slowing down the kinetics of the eutectic reaction and promoting the formation of the thicker lamella observed in the coarse $\gamma - \gamma'$ eutectic. Moreira et al.[45] indicated that the fine $\gamma - \gamma'$ structure presented a hypoeutectic composition, while the coarse interdendritic $\gamma - \gamma'$ structure showed a hypereutectic composition. These results explained the

changes in the proportion and size of the γ' phase in the interdendritic $\gamma - \gamma'$ structure.

Figure 6b also indicates that the primary γ dendrite in contact with the last liquid to solidify presents a region free of γ' precipitates. This result is in agreement with the previous work of Matache et al.,[46] who showed the formation of a Cr-rich film of γ phase between the primary γ dendrites and the interdendritic $\gamma - \gamma'$ structure. Figure 6c presents the $\gamma - \gamma'$ duplex microstructure in the core of the primary γ dendrite, showing submicron cuboidal γ'

Element	DV 106 heat	DV 109 heat	AMS 5391D standard[38]
Cr	**14.40**	**14.10**	12.0–14.0
C	0.10	0.10	0.08–0.20
Al	5.90	6.00	5.50–6.50
Mo	4.10	4.10	3.80–5.20
Nb	2.10	2.00	1.80–2.80
Ti	0.83	0.80	0.50–1.0
Fe	0.26	0.26	0.50 max.
Zr	0.07	0.06	0.05–0.15
Si	0.02	0.03	0.50 max.
B	0.010	0.010	0.005–0.015
Ta	0.06	0.05	Not specified
Co	< 0.01	< 0.01	1.0 max.
Cu	< 0.01	< 0.01	0.50 max.
Mn	< 0.01	< 0.01	0.25 max.
Ni	Balance	Balance	Balance

Bold values indicate the Cr-concentration values don't fit the specified range and that is relevant

precipitates within a γ matrix (see the microanalysis of the bulk primary γ' and the $\gamma - \gamma'$ partition of the duplex matrix in Table 2). The estimated fraction of γ' precipitates inside the dendrite of the as-cast microstructure was around 51%. The $\gamma \rightarrow (\gamma + \gamma')$ precipitation is usually incomplete during the cooling after the solidification,[47,48] and the usual γ' volume fraction in IN-713C castings is slightly above 50%.[6,13] Bhambri et al.[13] varied the casting conditions and processes to obtain a wide range of solidification conditions for an IN-713C alloy. The γ' proportion was around 52% (γ' size ~ 0.36 μm, SEM), and they concluded that "the precipitation of γ' went to completion in all specimens and that the cooling rate, within limits attained in these castings, had no effect on the resulting volume percentage of γ' in the alloy." They also mentioned that small differences in the proportion of γ' phase at the dendrite's center and boundary could be attributed to microsegregation. Ges et al.[20] observed a higher fraction of γ' precipitates (~ 60%, γ' size ~ 0.70 μm, SEM) in a 66-mm-diameter ingot of IN-713C. Zupanič et al.[11] also observed a higher volume fraction of γ' precipitates (at least 70%, γ' size ~ 50 nm, TEM) in the microstructure of a 10-mm-diameter IN-713C rod produced by continuous casting. According to Jackson et al.,[48] the fraction of γ' precipitates in the as-cast microstructure (see Figure 2c) is governed by thermodynamic and kinetic aspects, such as the alloy composition, the cooling rate, and the diffusion and the partitioning of alloying elements. The average width of the cuboid γ' precipitates in the as-cast microstructure was 910 ± 280 nm, and the width of the γ channels was around 230 ± 100 nm. The larger size (~ 0.91 μm) of the γ' precipitates and γ channels (~ 0.28 μm) in the present

(a)
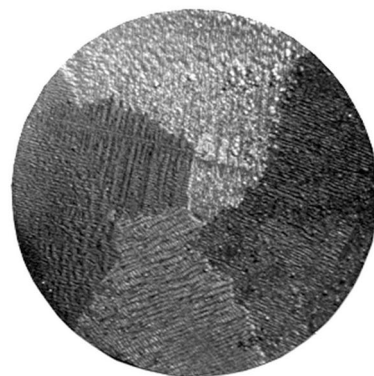


(b)

Figure 5. Macrostructure, DV 109 heat. (a) General view of the as-cast test pieces; (b) transversal macrography of the as-cast test pieces showing grain size of approximately 1400 μm (etching: $3HCl + 1H_2O_2$).

investigation when compared to previous results[13,28] might be explained by changes in the casting conditions, including the IN-713C chemical composition.

Table 3 shows that the room temperature tensile properties of as-cast IN-713C of DV106 and DV109 heats are within the requirements of the AMS 5391D standard.[38] Figure 7a shows a longitudinal view of the room temperature tensile testing sample. The fracture profile can be divided into four regions according to each grain. The fracture profiles of the left and central grains are rougher, featuring interdendritic crack propagation, possibly associated with the presence of intergranular porosities. The grain to the right features a straighter crack propagation (angle of approximately 60° to the tensile strength) propagation. Figure 7b shows interdendritic secondary cracking associated with as-cast porosities (see arrow). Figure 7c shows ductile (presence of dimples, see arrow 1) and brittle fractures (see arrow 2),
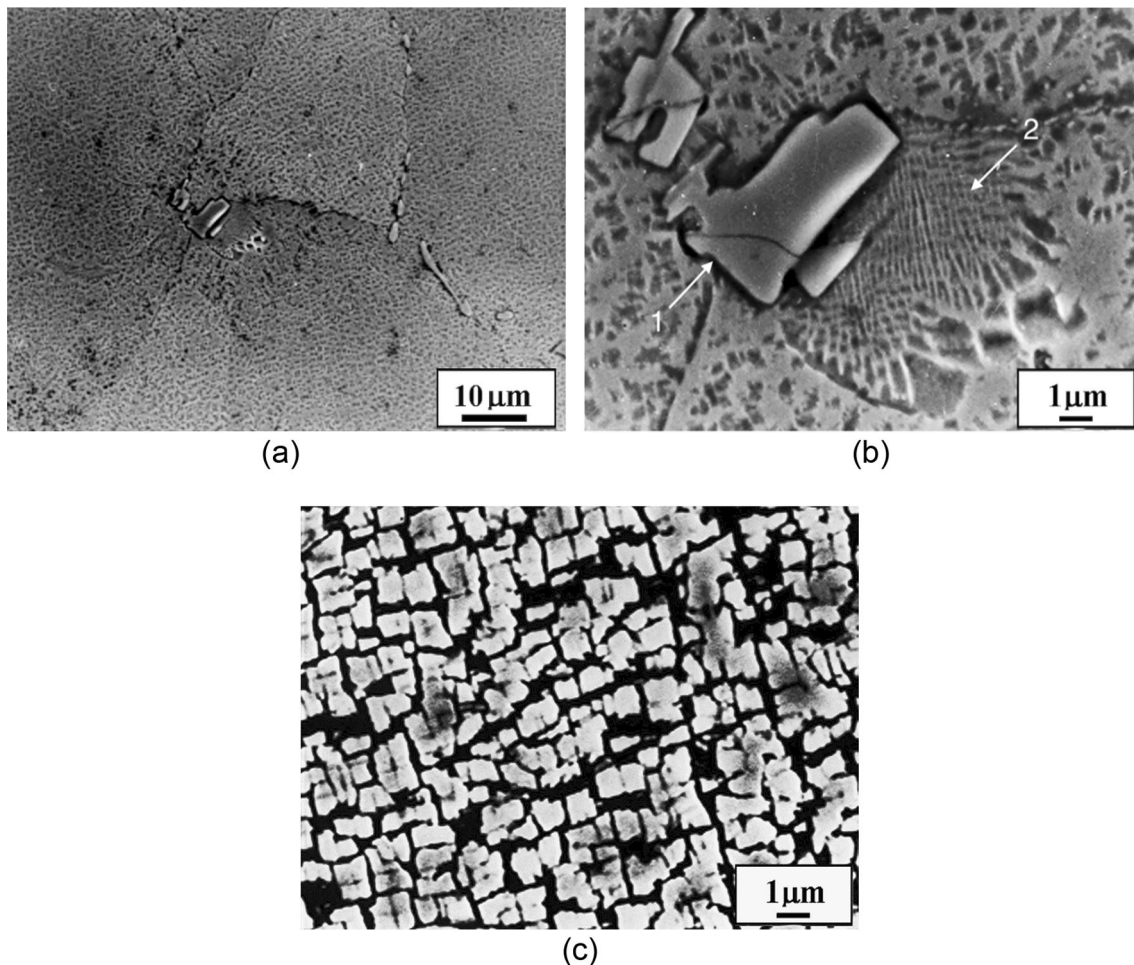
Figure 6. *Microstructural examination of the DV 109 samples, longitudinal section. (a) as-cast condition, large γ grains and interdendritic precipitation of faced and elongated (Mo, Nb, Cr)C carbides (size around 5 × 15 μm). Etching: glyceregia; (b) as-cast condition, detail showing interdendritic precipitation of (Mo, Nb, Cr)C carbides (light phase, see arrow 1), fine and coarse interdendritic γ − γ′ structure (see arrow 2) and cuboid γ′ precipitates (dark area). Etching: glyceregia. (c) as-cast condition, the core of a primary γ dendrite, detail of the intragranular cuboid γ′ precipitates (51% in area of γ′ phase, see light area) in the γ matrix (dark area). Etching: electrolytic: SEM, SEI.*

and the presence of secondary intergranular cracking (see arrow 3). Figure 7d shows the cleavage and secondary cracking of the interdendritic MC carbide (size of approximately 5 × 15 μm), indicating that the carbide fracture took place instead of the metal-carbide interfacial debonding. Similar cleavage of the MC carbide with numerous secondary cracks was previously reported in superalloys and iron.[49–51] MC carbides preferentially cleave on {100} planes, presenting, in the case of TiC, a brittle behavior at temperatures below 800 °C.[52–54] Figure 7e shows the ductile fracture details, featuring submicron dimples, indicating the ductile transgranular fracture in the core of the primary γ dendrite. The microfractographic examination suggests that the rupture of the samples was nucleated at the interdendritic as-cast porosities. This initial process was followed by the cracking and cleavage fracture of the interdendritic MC carbides at

approximately 300 MPa. Finally, the plastic deformation and the ductile fracture of the as-cast IN-713C specimens took place transgranularly in the primary γ dendrites above 700 MPa.

Table 4 shows the 650 °C tensile properties of as-cast IN-713C alloy of DV106 and DV109 heats. Comparing these results with the tensile results at room temperature (see Table 3) confirms a trend that the yield and tensile strengths do not vary with temperature up to 650 °C, see Figure 8.[4] However, the tensile strength and elongation values are below the typical values.[4] Figure 9a shows a longitudinal view of the 650 °C tensile testing sample, indicating the fracture profile features an interdendritic crack path. Figure 9b shows the interdendritic fracture details, while Figure 9c shows ductile (presence of dimples, see arrow 1) and brittle fracture (see arrow 2).

Table 2. EDS microanalysis results (at.%, without including the carbon) of the main phases of the IN-713C alloy, as-cast condition and after thermal exposure[13,18,25,39–41]

Phase	Source	%Cr	%Al	%Mo	%Nb	%Ti	%Zr	%Ni
MC	**Present investigation (as-cast)**	**2.7**	**0.4**	**11.3**	**61.9**	**17.9**	**–**	**6.0**
	As-cast condition[13]	–	–	6.0	63.0	31.0	–	–
	As-cast condition[39]	1.5	0.9	13.9	59.5	11.8	7.4	5.0
	Present investigation (after 60 h at 982 °C)	**5.1**	**2.9**	**7.9**	**39.6**	**11.5**	**4.2**	**28.9**
	After creep at 982 °C[39]	2.5	1.0	10.0	57.5	14.0	7.5	7.5
	After creep at 850 °C[40]	8.1	13.2	6.9	33.3	17.4	–	21.1
γ', interdendritic structure	**Present investigation (as-cast)**	**5.0**	**12.3**	**–**	**2.1**	**2.4**	**1.1**	**77.1**
	As-cast[39]	4.2	15.9	1.3	3.4	2.3	1.0	71.9
γ, duplex matrix	**Present investigation (after 60 h at 982 °C)**	**17.5**	**7.0**	**3.0**	**–**	**0.9**	**–**	**70.3**
	As-cast condition[13]	23.1	11.6	3.7	–	1.1	–	60.5
	After 750 min at 950 °C[25]	24.4	8.1	3.9	–	0.1	–	63.5
γ', cuboid precipitate	**Present investigation (after 60 h at 982 °C)**	**11.3**	**10.7**	**2.2**	**–**	**1.3**	**–**	**73.3**
	As-cast condition[13]	19.8	16.3	–	1.2	1.2	–	61.5
	After 750 min at 950 °C[25]	3.0	19.0	2.0	1.0	1.0	–	73.0
$M_{23}C_6$	**Present investigation (after 60 h at 982 °C)**	**41.9**	**4.2**	**–**	**12.8**	**1.7**	**2.9**	**36.5**
	After creep at – 982 °C[39]	32.5	10.0	7.5	2.5	1.0	0.5	46.0
	After creep at 850 °C[40]	53.4	17.0	2.3	1.1	5.2	–	21.0
σ phase[a]	Extrapolated from the Ni–Cr–Mo at 1204 °C[18]	30.0–50.0	–	20.0–40.0	–	–	–	30.0–35.0

Values obtained experimentally are highlighted in bold to differentiate them from values found in literature

[a]Submicron particle size below the SEM–EDS microanalysis spatial resolution

Figure 9d shows MC carbides (approximately 5 × 15 μm) in the fracture surface. The lack of intense intergranular cracking of the MC carbide (see white arrow) suggests that the MC carbide fracture took place by metal-carbide interfacial debonding (see black arrow) rather than carbide cleavage. The transition-metal carbides feature a brittle behavior at room temperature,[53] but at temperatures from 800 to 1200 °C, they might present plastic deformation by slip before the fracture.[55–57] The plastic deformation of the MC carbide below the metallic matrix's yield strength would favor the debonding rather than the MC carbide's cleavage, as observed at room temperature (see Figure 7d). Figure 9e shows the ductile fracture details, featuring submicron dimples, indicating the ductile transgranular fracture in the core of the primary γ dendrite. The microfractographic examination (see Figure 9c and d) illustrates that the fracture of the samples tensile-tested at 650 °C was also nucleated at the interdendritic as-cast porosities, followed by the plastic deformation of the MC carbides and the debonding of the metal-MC carbides interfaces. Finally, the plastic deformation and the ductile fracture of the as-cast IN-713C specimens took place transgranularly in the primary γ dendrites above 700 MPa.

Table 3. Tensile testing at room temperature

Test piece	Yield strength (MPa)	Tensile strength (MPa)	Elongation (%)
DV 106 #9	798	870	4.0
DV 109 #3	722	769	6.4
DV 109 #4	743	763	3.3
Average	754	801	4.5
AMS 5391D[38]	> 689	> 758	> 3.0

Figure 10a and b shows the microstructural characterization of a sample after the mechanical testing at 982 °C and 152 MPa (time to rupture of 57 h). Figure 10a features interdendritic $M_{23}C_6$ carbides and pools of stabilized γ' phase (dark area) around the carbides. These observations are following previous results.[13,14,18,20–24] During the exposure at 982 °C for 57 h, see Figure 2a and b, there is an incomplete decomposition of the primary MC carbides into $M_{23}C_6$ carbides (M = Cr, Mo and Nb, see Table 2). As a result, there is an increase in the proportion of
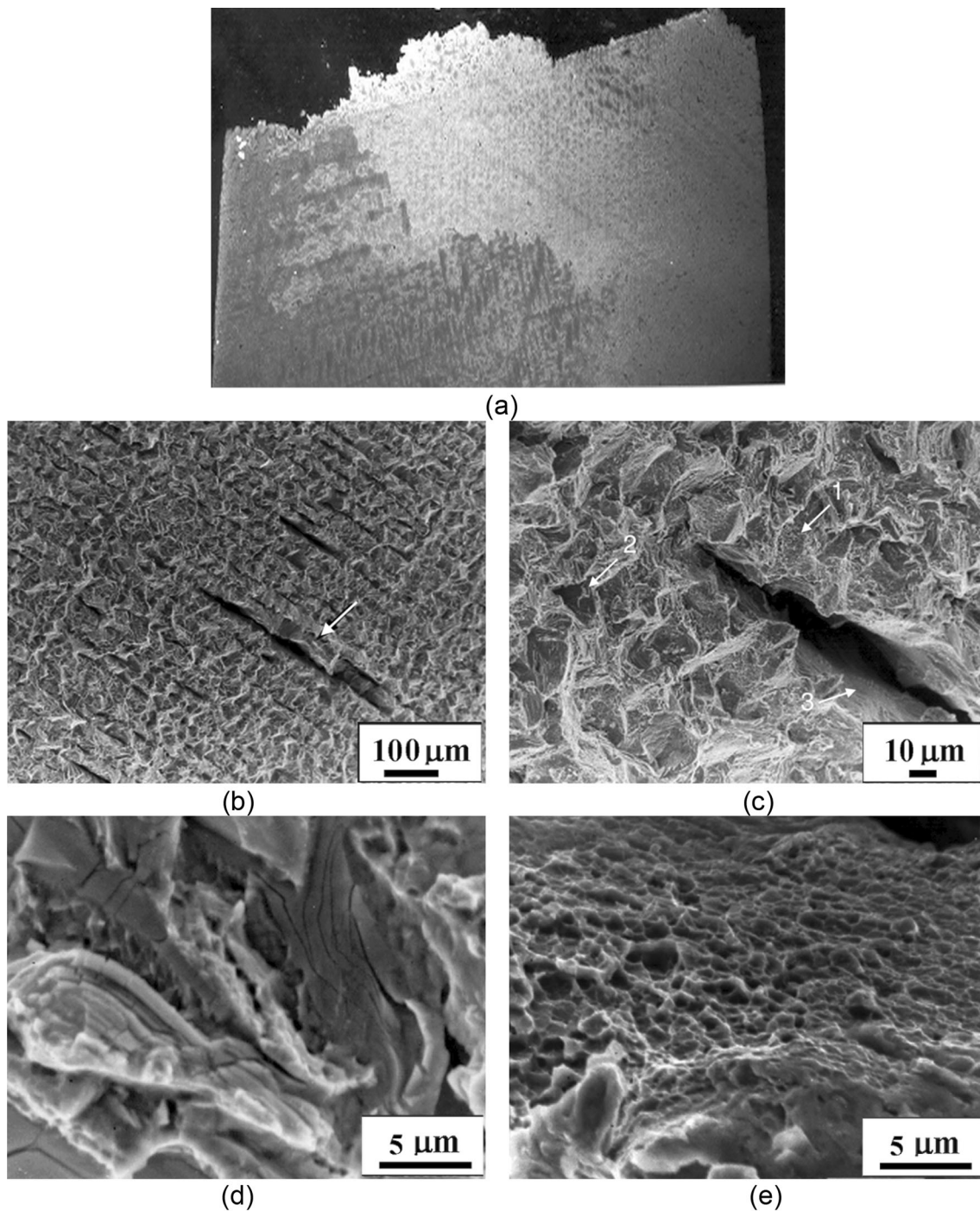
Figure 7. *Fractographic characterization after the room temperature tensile testing, DV109#4 sample. (a) general view near the fracture surface, showing a mixed fracture path with an interdendritic and a straighter crack propagation (stereomicroscope, longitudinal section, 18X, etching: glyceregia); (b) general view of the fracture surface showing secondary interdendritic cracking, probably due to the presence of interdendritic as-cast porosities. SEM; (c) detail showing ductile fracture (presence of submicron dimples, see arrow 1) and brittle fracture (see arrow 2), and secondary intergranular cracking (see arrow 3). SEM; (d) detail of intense secondary cracking and cleavage of the primary (Mo, Nb, Cr)C carbides. SEM; (e) detail of the ductile fracture showing submicron dimples in the core of a primary γ dendrite. SEM.*

intergranular carbides in the microstructure, see Figures 6a and 10a, from around 0.6–1.9 wt% (see Figure 11). The MC decomposition promotes the Nb-enrichment and Cr-depletion in the adjacent areas, leading to the growth and formation of γ' pools around the intergranular $M_{23}C_6$ carbides:[14,18,24] $(M, Nb)C + (Cr)\gamma \rightarrow (M, Cr)_{23}C_6 + (Nb)\gamma'$.

Table 4. Tensile testing at 650 °C

Test piece	Yield strength (MPa)	Tensile strength (MPa)	Elongation (%)
DV 106 #6	716	760	2.5
DV 109 #6	750	806	3.0
DV 109 #5	702	763	4.5
Average	723	776	3.3
Typical values[4]	718	867	6.7
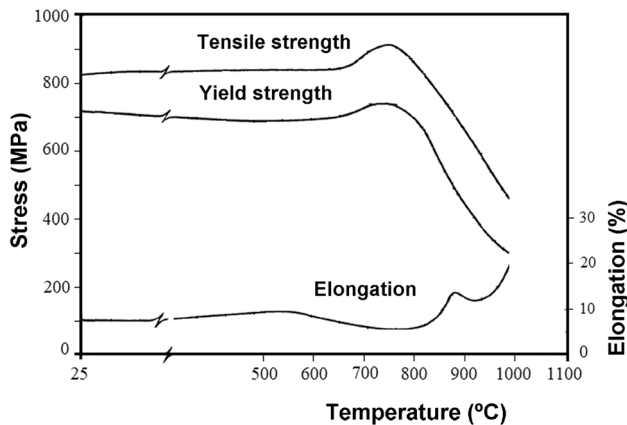
Figure 8. Typical tensile properties of as-cast vacuum-melted vacuum-cast IN-713C alloy, adapted from Ref. [4]. This figure was used with permission of The Nickel Institute (http://www.nickelinstitute.org); Engineering Properties of Alloys 713C, © 2020.

According to Mihalisin et al.,[18] $M_{23}C_6$ carbides are formed at the interfaces between the MC carbide and the surrounding γ' phase by the diffusion of Cr, Mo and C from the dissolving MC carbide. The diffusion of Ti and Nb from the dissolving MC carbide into the surrounding γ' creates the γ' phase islands. Both $M_{23}C_6$ carbides and γ' islands form preferentially around the decomposing MC particles. When the MC carbide becomes completely entrapped by the $M_{23}C_6$ carbides, the diffusion of Ti and Nb from MC to the γ' phase controls and delays the MC decomposition kinetics. In this sense, $M_{23}C_6$ and MC phases might cohabit in the microstructure of IN-713C during the stress-rupture testing at high temperatures (see the presence of MC and $M_{23}C_6$ carbides after 60 h at 982 °C in Table 2), confirming previous results.[58–60] Lvov et al.[58] studied the IN-738 blade from a gas turbine after a service of 26,000 h at 1080 °C. Guo et al.[59] investigated the cast Ni-based superalloy K452 microstructure evolution after heat treatment (up to 10,000 h at 900 °C). Azevedo and Hippert[60] investigated the IN-713C microstructure evolution after 200 h at 1000 °C. These investigations[58–60] observed the precipitation of $M_{23}C_6$ carbides and the degeneration of primary MC carbides, with both carbides coexisting in the microstructure after long thermal exposure.

Figure 10b shows the $\gamma - \gamma'$ duplex microstructure, featuring the rafting of the γ' precipitates (see light regions in this figure) in a γ matrix. According to the Thermo-Calc equilibria calculation (see Figure 2c), the proportion of γ' phase at 982 °C is around 39% in volume, close to measurement of 40%. The rafts presented an average width of 2.1 μm and a height of 0.4 μm. The corresponding average aspect ratio (height/width) of the γ' rafts is approximately 0.2, following the expected results for IN-713C for this testing condition.[61]

Figure 12a and b shows the microstructural characterization after the stress-rupture test at 815 °C and 305 MPa. Figure 12a features the precipitation of an acicular phase starting from the $M_{23}C_6$ carbide's interfaces, and no γ' pools were observed around these carbides. During the exposure at 815 °C for 831.4 h, there is a partial decomposition of the primary MC carbide into a discontinuous network of $M_{23}C_6$ carbides along the grain boundaries, see Figure 2a.[14,18,24] Figure 2a–c shows the formation of σ phase at temperatures below 900 °C. The TTT diagram of 713C alloy indicates that the precipitation of σ phase starts after 400 h at 815 °C, see Figure 2a.[18] This time is shorter than the exposure time at 815 °C in the present investigation, equals 831.4 h, indicating that the acicular phase observed in Figure 12a is the σ phase. Unfortunately, the spatial resolution of the EDS analysis was enough to check the submicron σ phase's chemical composition. According to Mihalisin et al.,[18] the acicular σ phase formed from an $M_{23}C_6$ carbide during the thermal exposure of IN-713C alloys is usually a Ni–Cr–Mo type (see Table 2), and the applied tensile stress accelerates its formation.

The conventional electron vacancy numbers of IN-713C alloy ($N_v \sim 2.25$ for DV106 heat and $N_v \sim 2.23$ for DV109 heat, see Table 1 and Eqn. 1) lie below the critical value of $N_v \sim 2.52$, which defines the Ni superalloys prone to σ phase formation.[18] The acicular σ phase formation was previously observed in an IN-713C alloy, featuring N_v of 2.15 after 500 h at 815 °C. Still, a similar IN-713C alloy with N_v of 2.14 did not show σ phase formation after the same thermal exposure.[18] Additionally, the sample with σ phase comparatively featured higher values of elongation, reduction of area and time to rupture, suggesting that the acicular σ phase precipitation does not cause any detrimental effect on the stress-rupture life of IN-713C.[18] For instance, a modified electron vacancy number equation (see Eqn. 2, which increases the weight of molybdenum and removes the effect of vanadium) provides higher N_v values for the IN-713C alloys ($N_v \sim 2.51$ for DV106 heat and $N_v \sim 2.50$ for DV109 heat), which suggest that the IN-713C is marginally prone to σ phase formation.[18] There are more models to predict the
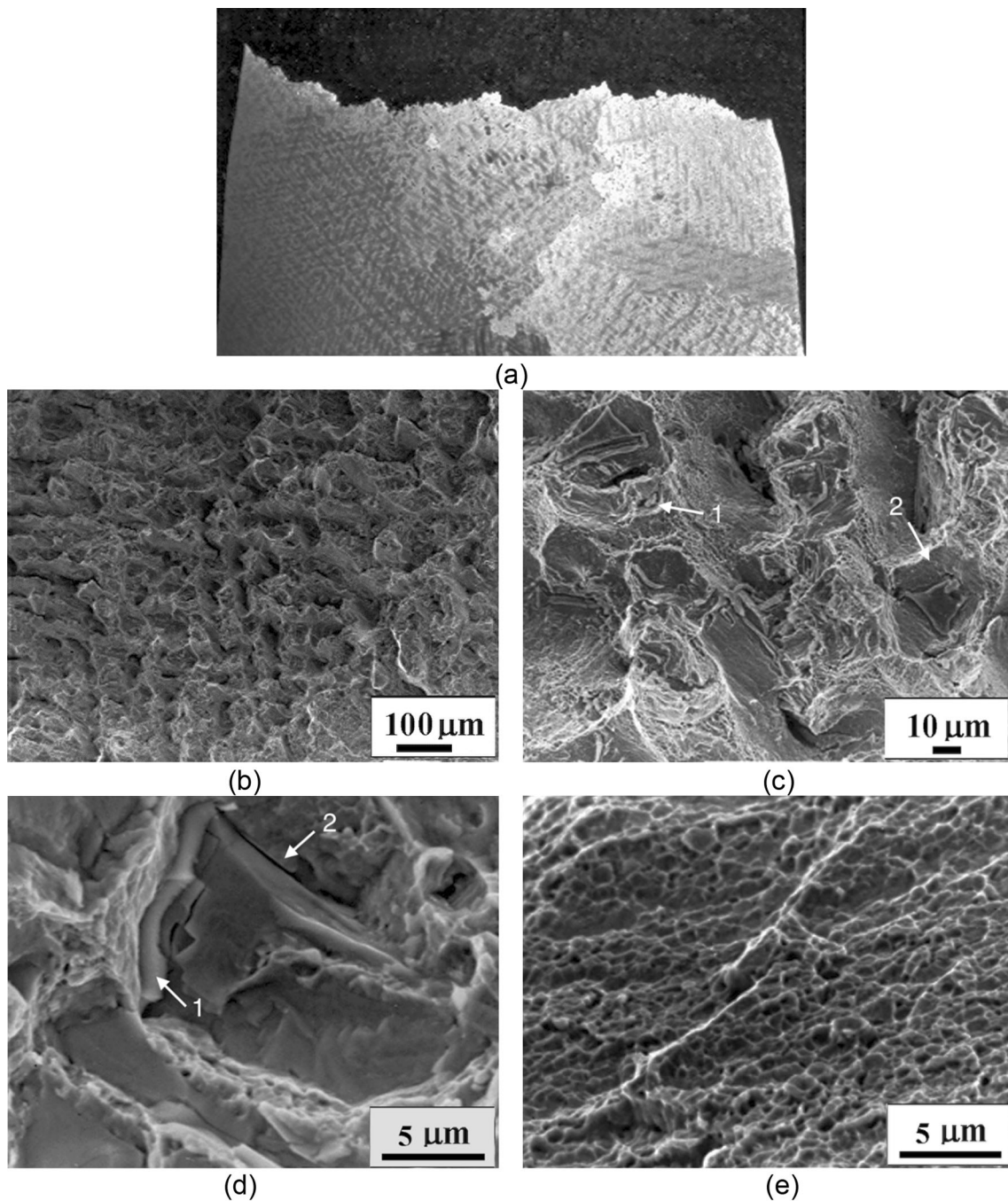
Figure 9. *Fractographic characterization after the 650 °C tensile testing, DV109#6. (a) general view near the fracture surface, showing an interdendritic crack path (stereomicroscope, longitudinal section, 18X, etching: glyceregia); (b) general view of the fracture surface showing interdendritic cracking. SEM; (c) detail showing ductile fracture (see arrow 1) and brittle fracture (see arrow 2). SEM (d) detail of the brittle fracture showing the MC carbide. Internal MC cracking is pointed by arrow 1, while the metal/MC debonding is identified by arrow 2. SEM; (e) detail of the ductile fracture surface, showing the presence of dimples. SEM.*

occurrence of topological close-packed in superalloys.[63] For instance, the PHACOMP method calculates and analyzes the parameter Md (which is an average energy level of d orbitals of the alloying transition metals). This parameter is related to their electronegativity atomic size and confirms that IN-713C is prone to σ phase formation.[62]

(a)

(b)
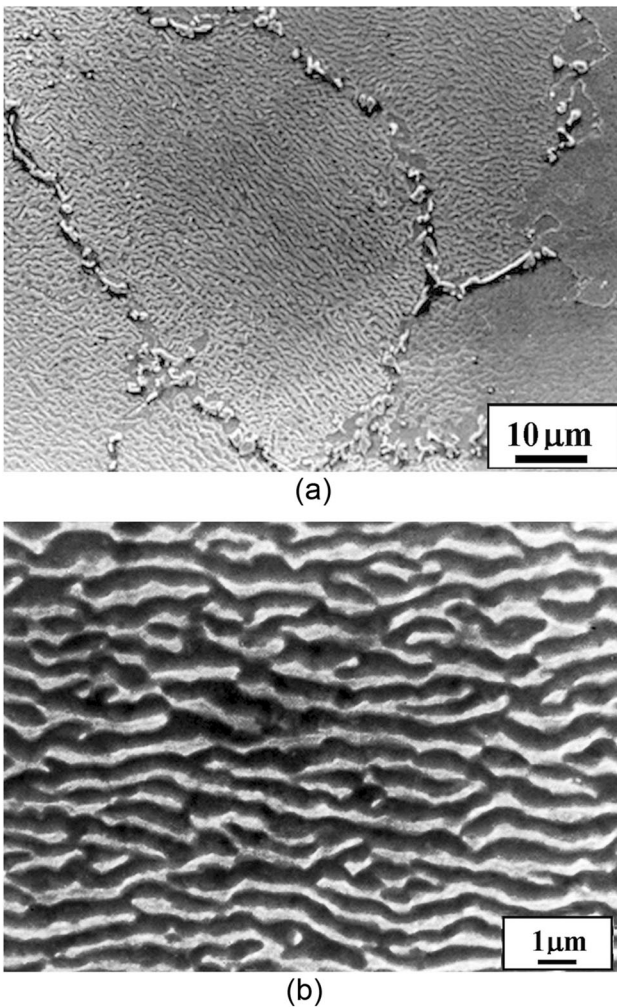
Figure 10. Microstructural characterization after the stress-rupture at 982 °C and 152 MPa, DV 106 #8, time to rupture of 57 h. (a) detail of the showing elongated γ′ precipitates (dark area) and intergranular $M_{23}C_6$ type carbides associated with MC carbides. Observe the formation of pools of the Nb-stabilized γ′ phase (dark-gray area) around the intergranular $M_{23}C_6$ carbides. SEM, longitudinal section, 1000 × , glyceregia etching; (b) detail of the γ + γ′ rafted microstructure. The elongated γ′ precipitates are represented by the light regions. The proportion of the γ′ phase was equal to 39%. SEM, longitudinal section, electrolytic etching.

$$N_v = 0.66\ \text{at.\%Ni} + 1.71\ \text{at.\%Co} + 2.66\ \text{at.\%Fe}$$
$$+ 4.66(\text{at.\%Cr} + \text{at.\%Mo} + \text{at.\%W}) \qquad \text{Eqn. 1}$$
$$+ 5.66\ \text{at.\%V} + 6.66\ \text{at.\%Zr}$$

$$N_v = 0.66\ \text{at.\%Ni} + 1.71\ \text{at.\%Co} + 2.66\ \text{at.\%Fe}$$
$$+ 4.66\ \text{at.\%Cr} + 6.66\ \text{at.\%Zr} \qquad \text{Eqn. 2}$$
$$+ 9.66(\text{at.\%Mo} + \text{at.\%W})$$

Figure 12b indicates the incomplete rafting of the γ′ precipitates at 815 °C and 305 MPa after 831.4 h. The γ′ particles' interfaces are still in a merging process, forming the entrapped γ phase in some regions (see circled areas in
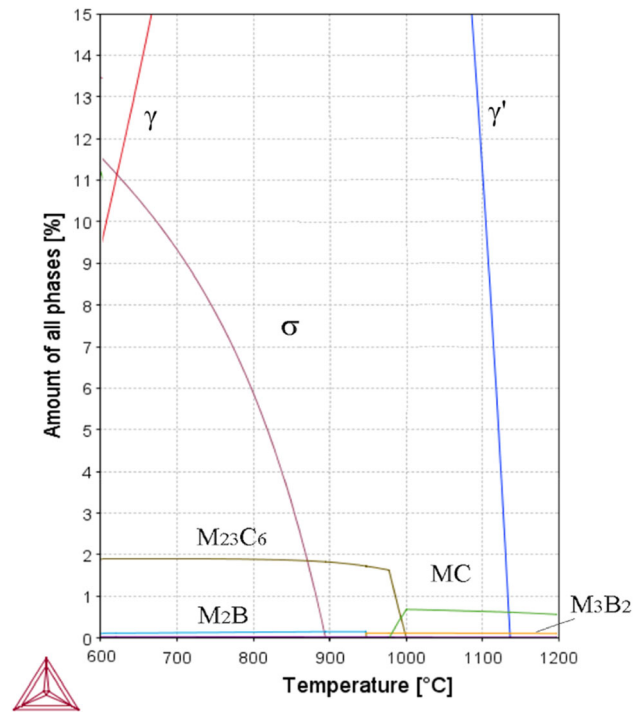
Figure 11. Minor phase concentration in equilibria in IN-713C alloy as a function of temperature, Thermo-Calc software.

Figure 12b). According to Thermo-Calc, the proportion of γ′ phase at 815 °C is around 60%, while the observed value is about 78%. These γ′ particles coarsened significantly compared to the as-cast microstructure (Figure 6c).

Table 5 shows the stress-rupture properties of the as-cast IN-713C samples tested at 152 MPa and 982 °C. The results of time to rupture and elongations follow the AMS 5391D standard.[38] Table 6 shows the stress-rupture properties of as-cast IN-713C samples tested at 305 MPa and 815 °C and the typical values.[4] The reduction of area and elongation results are slightly below these characteristic values. The elongation decrease in the samples tested at 815 °C is partially explained by the increase in the proportion of γ′ phase.[63,64] In both cases, the creep crack propagated intergranularly. Figure 13a shows the stress-rupture data of as-cast IN-713C, and the present results fit well with these data. Figure 13b shows the elongation for each temperature and rupture time. These values are scattered, but the data indicate that at lower testing temperatures, the elongation is smaller, due to the higher proportion of γ′ phase.

Figures 10a and 12b indicate the incomplete rafting of the γ′ precipitates at 815 °C and 305 MPa after 831.4 h. The applied stress in both temperatures is the same, approximately 50% of the yield stress. The slower rafting kinetics at lower temperatures was previously reported for a Co–9Al–9W–0.12B superalloy.[65] The authors stated that "it is evident that with increasing creep temperature, the
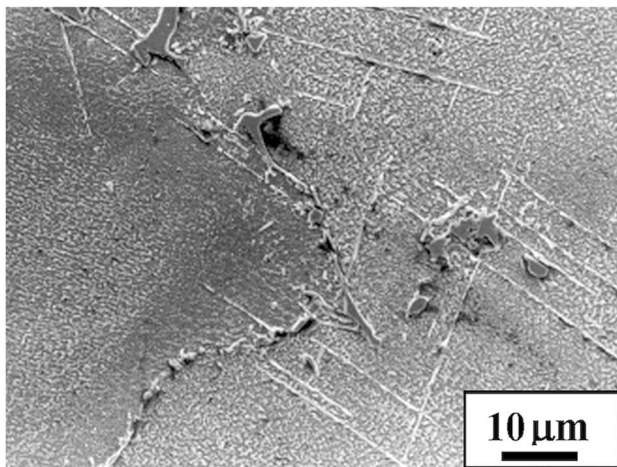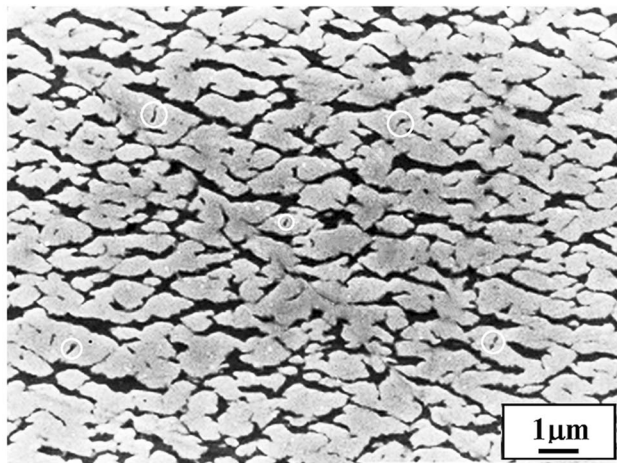
Figure 12. Microstructural characterization after the stress-rupture at 815 °C and 305 MPa, DV 109 #8, time to rupture of 831.4 h. (a) detail of the grain boundary precipitates showing $M_{23}C_6$ carbides associated with MC carbides, and precipitation of σ phase (acicular phase). SEM, longitudinal section, etching: Glyceregia; (b) detail of the γ + γ′ structure, which is partially rafted. The proportion of the γ′ phase was equal to 78%. White circles indicate few entrapped γ phase channels. In this etching, the γ′ precipitates are the light regions. SEM, longitudinal section, etching: electrolytic.

tendency to rafting increases." They explained that the diffusion kinetics was too slow at lower temperatures for pronounced directional coarsening in the "given creep time." Using the diffusion coefficients for Mo, Cr and Al in γ and γ′ phases,[66–68] the diffusion distances ($\sqrt{Dt}$, where "t" is the duration of each stress-rupture test and D is the diffusion coefficient at testing temperature) were estimated for each testing condition. These results indicated that the diffusion distances at 982 °C were approximately twice the values at 815 °C.

Figure 14a illustrates the initial rafting formation and shows the shortest diffusion paths of the alloying elements.

The γ′-forming elements must move from the perpendicular faces of the γ′ precipitates to the vertical faces, while the γ-forming elements travel from the vertical to the horizontal γ channels. The corners of adjacent γ′ precipitates may entrap the γ channels during this process.[69] The average size of the γ′ precipitates and the γ channel width (see Figure 14a) were estimated for each testing condition, based on the γ′ volumetric fraction at 815 °C (60%) and 982 °C (40%), see Figures 2c, 14b and c. The higher proportion of γ′ phase at 815 °C creates thinner γ channels, facilitating γ islands' formation, see circles in Figure 12b. The dissolution of these γ islands depends on the atomic diffusion in the γ′ phase,[68] which delays the rafting kinetics at lower testing temperatures. Reed et al.[69] also suggested that the smaller γ′ channel width promotes higher resistance to the rafting of the interdendritic regions of CMSX-4 alloy.

Moreover, the misfit between γ and γ′ phases tends to become more negative with increasing temperatures.[28–35,70] Therefore, the coherency stress and the creep plastic deformation in the horizontal γ channels are comparatively higher at 982 °C than 815 °C. The rafting driving force depends on the decrease of the γ − γ′ coherency stress in the horizontal γ channels, which takes place by the formation of γ − γ′ interfacial dislocation network.[2,28–35,71–73] The γ − γ′ dislocation network is formed by a series of thermally activated creep-dislocation
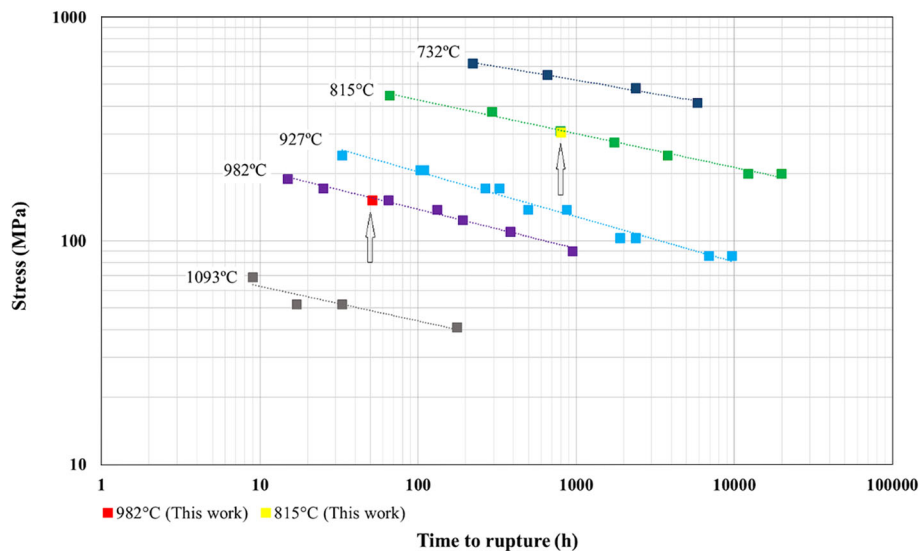
(a)
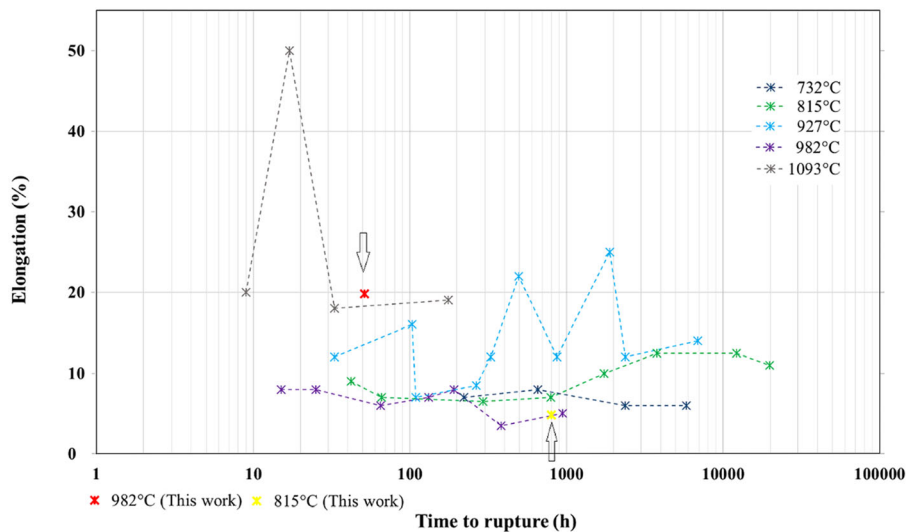
(b)

Figure 13. (a) Stress-rupture data on as-cast IN-713C; (b) elongation values for different temperatures and rupture times. Figures adapted from the Nickel Institute catalog.[4]

reactions, which feature a strong edge character and minimize the coherency stress in the horizontal γ channels.[2] At higher temperatures, the dislocation climb and dislocation cross-slip around the γ′ precipitates are favored,[74] promoting the formation of the γ − γ′ interfacial dislocations and, as a consequence, the rafting. Tables 5 and 6 show that the elongation at 982 °C was higher than at 815 °C (19.8 vs. 4.8%), indicating that the glide of the dislocations in the γ matrix was easier. Finally, when a polycrystalline superalloy is submitted to the stress-rupture test, some grains may present rafting, while others maintain the cuboid morphology of the γ′ precipitates.[75–77] Even inside a grain, the rafting kinetics near the interdendritic regions is slower due to the segregation and the higher proportion of γ′ phase and smaller γ channels,[69] see Figure 10a.

Conclusions

- The room temperature tensile properties were within the requirements of the AMS 5391D standard. The fracture was nucleated at the interdendritic as-cast porosities, followed by multiple cracking and cleavage fracture of the interdendritic MC carbides. The ductile fracture took place transgranularly in the primary γ dendrites.
- The 650 °C tensile properties and microfractographic features were similar to the results at room temperature. However, debonding of the metal/MC carbides interfaces rather than cleavage fracture of the MC carbides was observed.
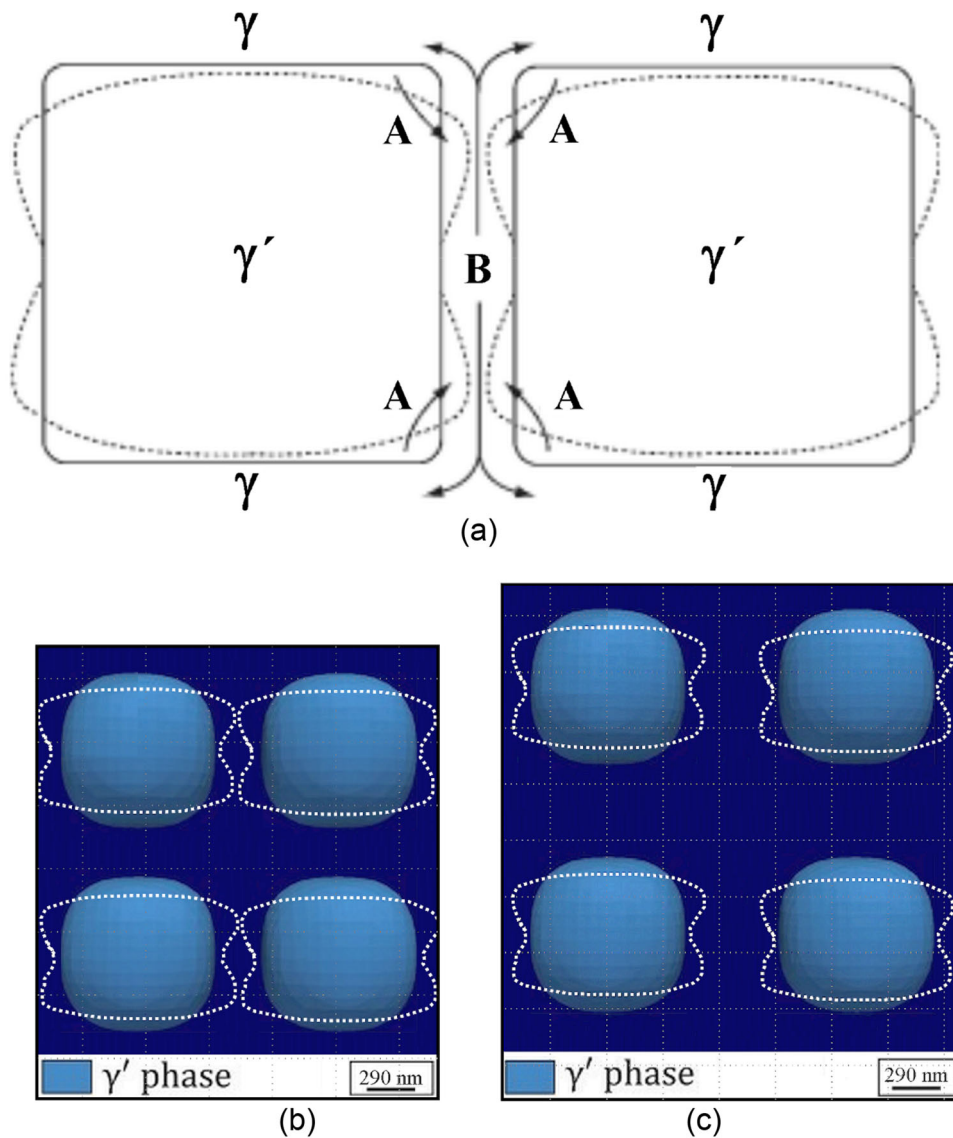
Figure 14. (a) Scheme is showing the rafting formation. "A" represents the γ'-forming elements and "B" the γ-forming elements. The shortest diffusion paths for A and B are indicated by the black arrows. "A" elements must move from the perpendicular faces of γ' precipitates to the vertical faces while "B" must travel from the vertical to the horizontal γ channels. The corners of adjacent γ' precipitates may entrap the γ channels during this process[69]; (b) and (c) extrapolated γ − γ' microstructure before rafting and after the same interfacial growth (dotted lines). The calculated γ channel width is based on the equilibrium fraction of γ' phase indicated by Thermo-Calc, γ' precipitate size is equal to 1.0 μm for both conditions: (b) 815 °C with γ' fraction equals to 60%, formation of γ islands; (c) 982 °C with γ' fraction equals to 40%. (a) Was used with the permission of Taylor and Francis Group on behalf of the Institute of Materials, Minerals and Mining; Materials Science and Technology, Reed et al., Kinetics of rafting in a single crystal superalloy: effects of residual microsegregation, © 2007

- The stress-rupture properties at 982 °C and 152 MPa were within the requirements of the AMS 5391D standard. The microstructure featured an incomplete transformation of MC carbides into $M_{23}C_6$ carbides and γ' pools. The γ − γ' microstructure featured rafting with a proportion of γ' phase equals to 39%.

- The microstructure after the stress-rupture properties at 815 °C and 305 MPa additionally featured acicular σ phase precipitates and absence of γ' pools around the carbides. The γ − γ' duplex microstructure showed incomplete rafting due to the formation of entrapped γ channels, as the proportion of γ' phase was equal to 78%.

REFERENCES

1. C.T. Sims, N.S. Stoloff, W.C. Hagel, *Superalloys II: High-Temperature Materials for Aerospace and Industrial Power* (Wiley, New York, 1987)
2. R.C. Reed, *The Superalloys: Fundamentals and Applications* (Cambridge University Press, Cambridge, 2006)
3. M.J. Donachie, S.J. Donachie, Superalloys, in *Metals Handbook Desk Edition*, 2nd edn., ed. by J.R. Davis (ASM International, Cleveland, 1998), pp. 394–414. https://doi.org/10.31399/asm.hb.mhde2.a0003120
4. Engineering Properties of Alloys 713C. (Nickel Institute, Technical Guides 2020). https://www.nickelinstitute.org/media/4686/ni_inco_337_engineering713.pdf
5. C.G. Bieber, W.F. Sumpter, Inventors 1951 Oct. 09. *High-Temperature Alloys and Articles*. United States patent US 2,570,193A
6. J.Y. Song. *Microstructure Control and Improvement of Ductility of IN-713C alloy with and without Co Addition*. Ph.D. Thesis, Tohoku University (2015). https://tohoku.repo.nii.ac.jp/?action=repository_uri&item_id=71478&file_id=18&file_no=1
7. J. Nawrocki, M. Motyka, D. Szeliga, W. Ziaja, R. Cygan, J. Sieniawski, Effect of cooling rate on macro- and microstructure of thin-walled nickel superalloy precision castings. Journal of Manufacturing Processes. **49**, 153–161 (2020). https://doi.org/10.1016/j.jmapro.2019.11.028
8. M. Azadi, M. Azadi, Evaluation of high-temperature creep behavior in Inconel-713C nickel-based superalloy considering effects of stress levels. Mater. Sci. Eng., A **689**, 298–305 (2017). https://doi.org/10.1016/j.msea.2017.02.066
9. S. Zlá et al., Determination of thermophysical properties of high temperature alloy IN713LC by thermal analysis. J. Therm. Anal. Calorim. **110**, 211–219 (2012). https://doi.org/10.1007/s10973-012-2304-8
10. A.G.J. Santos. *Simulação termodinâmica da superliga a base de níquel Inconel 713C*. Master Thesis, University of São Paulo (2012). https://teses.usp.br/teses/disponiveis/97/97134/tde-01102013-093600/publico/EMD12001_C.pdf
11. F. Zupanič, T. Bončina, A. Križman, F.D. Tichelaar, Structure of continuously cast Ni-based superalloy Inconel 713C. J. Alloys Compd. **329**, 290–297 (2001). https://doi.org/10.1016/S0925-8388(01)01676-0
12. J.R. Brinegar, J.R. Mihalisin, J. VanderSluis. The effect of tantalum for columbium substitutions in alloy 713C. Superalloys 53–62 (1984). https://www.tms.org/superalloys/10.7449/1984/Superalloys_1984_53_61.pdf
13. A.K. Bhambri, T.Z. Kattamis, J.E. Morral, Cast microstructure of Inconel 713C and its dependence on solidification variables. Metall. Trans. B **6**, 523–537 (1975). https://doi.org/10.1007/BF02913844
14. G.P. Sabol, R. Stickler, Microstructure of Nickel-based superalloys. Phys. Stat. Sol. B **35**, 11–52 (1969). https://doi.org/10.1002/pssb.19690350102
15. J.F. Radavich, Effects of Zr Variations on the Microstructural Stability of Alloy 713C, in *Proceedings of the First International Symposium on Structural Stability in Superalloys* (Vol. 1, Sept. 1968)
16. J. Morrow, F.R. Tuler, Low cycle fatigue evaluation of Inconel 713C and waspaloy. ASME. J. Basic Eng. **87**, 275–289 (1965). https://doi.org/10.1115/1.3650539
17. T. Murakumo, T. Kobayashi, Y. Koizumi, H. Harada, Creep behaviour of Ni-base single-crystal superalloys with various γ' volume fraction. Acta Mater. **52**, 3737–3744 (2004). https://doi.org/10.1016/j.actamat.2004.04.028
18. J.R. Mihalisin, C.G. Bieber, R.T. Grant, Sigma-it's occurrence, effect, and control in nickel-base

superalloys. Trans. Metall. Soc. AIME. **242**, 2399–2414 (1968)

19. D. Gelmedin et al., Fatigue behavior of the superalloy IN713C under LCF, HCF and superimposed LCF/HCF loading. Proc. Eng. **2**, 1343–1353 (2010). https://doi.org/10.1016/j.proeng.2010.03.146

20. A. Ges, H. Palacio, R. Versaci, IN-713C characteristic properties optimized through different heat treatments. J. Mater. Sci. **29**, 3572–3576 (1994). https://doi.org/10.1007/BF00352065

21. S. Safarloo, F. Loghman, M. Azadi, M. Azadi, Optimal design experiment of ageing time and temperature in Inconel-713C superalloy based on hardness objective. Trans. Indian Inst. Met. **71**, 1563–1572 (2018). https://doi.org/10.1007/s12666-018-1291-2

22. M. Azadi, A. Marbout, S. Safarloo, M. Azadi, M. Shariat, M.H. Rizi, Effects of solutioning and ageing treatments on properties of Inconel-713C nickel-based superalloy under creep loading. Mater. Sci. Eng., A **711**, 195–204 (2018). https://doi.org/10.1016/j.msea.2017.11.038

23. B.B. Galizoni, A.A. Couto, D.A.P. Reis, Heat treatments effects on nickel-based superalloy Inconel 713C. Metals **9**, 47 (2019). https://doi.org/10.3390/met9010047

24. G.F. Vander Voort, *Atlas of Time-Temperature Diagrams for Nonferrous Alloys* (ASM International, Cleveland, 1991)

25. A. Somoza, G. Santos, A. Ges, R. Versaci, F. Plazaola, Age-hardening and precipitation phenomena in the Inconel-713C superalloy studied by means of positron lifetime spectroscopy. Phys. Stat. Sol. A **174**, 189 (1999). https://doi.org/10.1002/(sici)1521-396x(199907)174:1%3c189:aid-pssa189%3e3.0.co;2-y

26. H.E. Collins, Relative long-time stability of carbide and intermetallic phases in nickel-base superalloys, in *Proceedings of the International Symposium on the Structural Stability in* Superalloys (American Society for Metals and American Institute of Mining, Metallurgical, and Petroleum Engineers, 1968), pp. 171–198. https://www.tms.org/Superalloys/10.7449/1968/Superalloys_1968_171_198.pdf

27. H. Matysiak et al., The microstructure degradation of the IN 713C Nickel-based superalloy after the stress rupture tests. J. Mater. Eng. Perform. **23**, 3305–3313 (2014). https://doi.org/10.1007/s11665-014-1123-4

28. M.A. Ali, J.V. Görler, I. Steinbach, Role of coherency loss on rafting behavior of Ni-based superalloys. Comput. Mater. Sci. **171**, 109279 (2020). https://doi.org/10.1016/j.commatsci.2019.109279

29. W.P. Wu, S.Y. Li, Y.L. Li, An anisotropic elastic–plastic model for predicting the rafting behavior in Ni-based single crystal superalloys. Mech. Mater. **132**, 9–17 (2019). https://doi.org/10.1016/j.mechmat.2019.02.009

30. R. Desmorat, A. Mattiello, J. Cormier, A tensorial thermodynamic framework to account for the γ' rafting in nickel-based single crystal superalloys. Int. J. Plast **95**, 43–81 (2017). https://doi.org/10.1016/j.ijplas.2017.03.010

31. Y. Tsukada, T. Koyama, F. Kubota, Y. Murata, Y. Kondo, Phase-field simulation of rafting kinetics in a nickel-based single crystal superalloy. Intermetallics **85**, 187–196 (2017). https://doi.org/10.1016/j.intermet.2017.02.017

32. J. Coakley, D. Ma, M. Frost, D. Dye, D.N. Seidman, D.C. Dunand, H.J. Stone, Lattice strain evolution and load partitioning during creep of a Ni based superalloy single crystal with rafted γ' microstructures. Acta Mater. **135**, 77–87 (2017). https://doi.org/10.1016/j.actamat.2017.06.021

33. R.C. Reed, N. Matan, D.C. Cox, M.A. Rist, C.M.F. Era, Creep of CMSX-4 superalloy single crystals: effects of rafting at high temperature. Acta Mater. **47**, 3367–3381 (1999). https://doi.org/10.1016/S1359-6454(99)00217-7

34. N. Matan, D.C. Cox, C.M.F. Rae, R.C. Reed, On the kinetics of rafting in CMSX-4 superalloy single crystals. Acta Mater. **47**, 2031–2045 (1999)

35. F.R.N. Nabarro, Rafting in Superalloys. Metall. Mater. Trans. A **27**, 513–530 (1996). https://doi.org/10.1007/BF02648942

36. ASTM E8/E8M-16ae1, *Standard Test Methods for Tension Testing of Metallic Materials* (ASTM International, West Conshohocken PA, 2016)

37. ASTM E21-17e1, *Standard Test Methods for Elevated Temperature Tension Tests of Metallic Materials* (ASTM International, West Conshohocken PA, 2017)

38. SAE AMS 5391D. Nickel Alloy, Corrosion and Heat Resistant, Investment Castings, 73Ni–13Cr–4.5Mo–2.3Cb–0.75Ti–6.0Al–0.010B–0.10Zr Vacuum Cast, As-Cast, Society of Automobile Engineers (Aerospace Material Specifications, Warrendale PA, 1995) https://doi.org/10.4271/ams5391d

39. Ł. Rakoczy, M. Grudzień, R. Cygan, Influence of melt-pouring temperature and composition of primary coating of shell mold on tensile strength and creep resistance of Ni-based superalloy. J. Mater. Eng. Perform. **28**, 3826–3834 (2019). https://doi.org/10.1007/s11665-018-3853-1

40. M. Azadim, M. Azadi, A.H. Mohammadi, Effects of ageing and forging on short-term creep behaviors of Inconel-713C superalloy at 850 & #xB0;C. IJE Trans A Basics **33**, 639–646 (2020). https://doi.org/10.5829/ije.2020.33.04a.15

41. M. Lachowicz, W. Dudziński, Non-equilibrium decomposition of MC carbides in superalloy Inconel 713C Melted with Welding Techniques. Arch. Metall. Mater. **55**, 305–315 (2010)

42. N. Warnken, Studies on the solidification path of single crystal superalloys. J. Phase Equilibr. Diffus.

37, 100–107 (2016). https://doi.org/10.1007/s11669-015-0445-8

43. A. Heckl, R. Rettig, S. Cenanovic, M. Göken, R.F. Singer, Investigation of the final stages of solidification and eutectic phase formation in Re and Ru containing nickel-base superalloys. J. Cryst. Growth **312**, 2137–2144 (2010). https://doi.org/10.1016/j.jcrysgro.2010.03.041

44. F. Wang, D. Ma, A. Bührig-Polaczek, Preferred growth orientation and microsegregation behaviors of eutectic in a nickel-based single-crystal superalloy. Sci. Technol. Adv. Mater. **16**, 025004 (2015). https://doi.org/10.1088/1468-6996/16/2/025004

45. M.F. Moreira, L.B. Fantin, C.R.F. Azevedo, Microstructural characterization of Ni superalloy as-cast single-crystal (CMSX-4). Int. J. Metalcast. (2020). https://doi.org/10.1007/s40962-020-00496-1

46. G. Matache, D.M. Stefanescu, C. Puscasu, E. Alexandrescu, Dendritic segregation and arm spacing in directionally solidified CMSX-4 superalloy. Int. J. Cast Met. Res. **29**, 303–316 (2016). https://doi.org/10.1080/13640461.2016.1166726

47. R. Kozubski, Long-range order kinetics in Ni3Al-based intermetallic compounds with L12-type superstructure. Prog. Mater Sci. **41**, 1–59 (1997). https://doi.org/10.1016/S0079-6425(97)00002-9

48. M.P. Jackson, M.J. Starink, R.C. Reed, Determination of the precipitation kinetics of Ni3Al in the Ni–Al system using differential scanning calorimetry. Mater. Sci. Eng., A **264**, 26–38 (1999). https://doi.org/10.1016/S0921-5093(98)01120-4

49. C. McMahon, M. Cohen, Initiation of cleavage in polycrystalline iron. Acta Metall. **13**, 591–604 (1965). https://doi.org/10.1016/0001-6160(65)90121-5

50. Y. Zhang, X. Cao, P. Wanjara, M. Medraj, Tensile properties of laser additive manufactured Inconel 718 using filler wire. J. Mater. Res. **29**, 2006–2020 (2014). https://doi.org/10.1557/jmr.2014.199

51. Y. Liu et al., Fracture mechanisms induced by microporosity and precipitates in isothermal fatigue of polycrystalline nickel based superalloy. Mater. Sci. Eng., A **736**, 438–452 (2018). https://doi.org/10.1016/j.msea.2018.06.095

52. L. Toth. Transition Metal Carbides and Nitrides

53. H.O. Pierson, *Handbook of Refractory Carbides and Nitrides* (Noyes Publication, New Jersey, 1996)

54. Y.Z. Liu, Y.H. Jiang, J. Feng, R. Zhou, Elasticity, electronic properties and hardness of MoC investigated by first principles calculations. Phys. B **419**, 45–50 (2013). https://doi.org/10.1016/j.physb.2013.03.016

55. D.J. Rowcliffe, G.E. Hollox, Hardness anisotropy, deformation mechanisms and brittle-to-ductile transition in carbide. J. Mater. Sci. **6**, 1270–1276 (1971). https://doi.org/10.1007/BF00552040

56. W.S. Williams, Influence of temperature, strain rate, surface condition, and composition on the plasticity of transition-metal carbide crystals. J. Appl. Phys. **35**, 1329–1338 (1964). https://doi.org/10.1063/1.1713614

57. D.L. Kohlstedt, The temperature dependence of microhardness of the transition-metal carbides. J. Mater. Sci. **8**, 777–786 (1973). https://doi.org/10.1007/BF02397907

58. G. Lvov, V.I. Levit, M.J. Kaufman, Mechanism of primary MC carbide decomposition in Ni-base superalloys. Metall. Mater. Trans. A **35**, 1669–1679 (2004). https://doi.org/10.1007/s11661-004-0076-x

59. X.Z. Qin, J.T. Guo, C. Yuan, C.L. Chen, J.S. Hou, H.Q. Ye, Decomposition of primary MC carbide and its effects on the fracture behaviors of a cast Ni-base superalloy. Mater. Sci. Eng., A **485**, 74–79 (2008). https://doi.org/10.1016/j.msea.2007.07.055

60. C.R.F. Azevedo, E. Hippert Jr, Activities of the microstructure and mechanical testing groups, in *LMAF-JICA 02-96 Report, JICA Project in Nickel base Superalloys* (Instituto de Pesquisas Tecnológicas do Estado de São Paulo, 1996)

61. J. Ohe, S. Wakita, Practical method of thermal history analysis by γ' morphology. Superalloys **1984**, 93–102 (1984)

62. M. Morinaga, N. Yukawa, H. Adachi, H. Ezaki, New PHACOMP and its application to alloy design. Superalloys **1984**, 523–532 (1984)

63. T.P. Weihs, V. Zinoviev, D.V. Viens, E.M. Schulson, The strength, hardness and ductility of Ni$_3$Al with and without boron. Acta Metall. **35**, 1109–1118 (1987). https://doi.org/10.1016/0001-6160(87)90058-7

64. Q. Yao et al., Phase stability, elastic, and thermodynamic properties of the L12 (Co, Ni)3(Al, Mo, Nb) phase from first-principles calculations. J. Mater. Res. **32**, 2100–2108 (2017). https://doi.org/10.1557/jmr.2017.8

65. A. Bauer, S. Neumeier, F. Pyczak, M. Göken, Creep strength and microstructure of polycrystalline γ'-strengthened cobalt-base superalloys. Superalloys **12**, 695–703 (2012). https://doi.org/10.1002/9781118516430.ch77

66. C.Z. Hargather, S.L. Shang, Z.K. Liu, Data set for diffusion coefficients and relative creep rate ratios of 26 dilute Ni-X alloy systems from first-principles calculations. Data Brief. **20**, 1537–1551 (2018). https://doi.org/10.1016/j.dib.2018.08.144

67. C.E. Campbell, W.J. Boettinger, U.R. Kattner, Development of a diffusion mobility database for Ni-base superalloys. Acta Mater. **50**, 775–792 (2002). https://doi.org/10.1016/S1359-6454(01)00383-4

68. Y. Minamino, H. Yoshida, S.B. Jung, K. Hirao, T. Yamane, Diffusion of Platinum and Molybdenum in Ni and Ni3Al. Defect Diffusion Forum **143–147**, 257–262 (1997). https://doi.org/10.4028/www.scientific.net/ddf.143-147.257

69. R.C. Reed, D.C. Cox, C.M.F. Rae, Kinetics of rafting in a single crystal superalloy: effects of residual

microsegregation. Mater. Sci. Technol. **23**, 893–902 (2007). https://doi.org/10.1179/174328407X192723

70. A.J. Goodfellow, L.R. Owen, K.A. Christofidou, J. Kelleher, M.C. Hardy, H.J. Stone, The effect of temperature and Mo content on the lattice misfit of model Ni-based superalloys. Metals **9**, 700 (2019). https://doi.org/10.3390/met9060700

71. R.D. Field, T.M. Pollock, W.H. Murphy, The development of γ/γ' interfacial dislocation networks during creep in Ni-base superalloys. Superalloy **192**, 557–566 (1992)

72. B. Liu, D. Raabe, F. Rotes, A. Arsenlis, Interfacial dislocation motion and interactions in single-crystal superalloys. Acta Mater. **79**, 216–233 (2014). https://doi.org/10.1016/j.actamat.2014.06.048

73. S. Sulzer et al., On the assessment of creep damage evolution in nickel-based superalloys through correlative HR-EBSD and cECCI studies. Acta Mater. **185**, 13–27 (2020). https://doi.org/10.1016/j.actamat.2019.07.01

74. M. Kamaraj, V.M. Radhakrishnan, First report on the deformation mechanism mapping of first and second generation Ni-based single crystal super alloys. Trans. Indian Inst. Met. **70**, 2485–2496 (2017). https://doi.org/10.1007/s12666-017-1120-z

75. J. Hakl, T. Vlasák, J. Lapin, Creep behaviour and microstructural stability of cast nickel based superalloy IN 792 5A. Kovove Mater. **45**, 177–188 (2007)

76. M. Yang et al., Study of γ' rafting under different stress states – A phase-field simulation considering viscoplasticity. J. Alloys Compd. **769**, 453–462 (2018). https://doi.org/10.1016/j.jallcom.2018.07.317

77. H. Yu et al., Microstructure evolution and creep behavior of a [111] oriented single crystal nickel-based superalloy during tensile creep. Mater. Sci. Eng., A **565**, 292–300 (2013). https://doi.org/10.1016/j.msea.2012.12.015